SCIENTIFIC REPORTS

OPEN

Observation of microwave absorption and emission from incoherent electron tunneling through a normal-metal–insulator–superconductor junction

Shumpei Masuda[1], Kuan Y. Tan[1], Matti Partanen[1], Russell E. Lake[1], Joonas Govenius[1], Matti Silveri[1,2], Hermann Grabert[3] & Mikko Möttönen[1]

We experimentally study nanoscale normal-metal–insulator–superconductor junctions coupled to a superconducting microwave resonator. We observe that bias-voltage-controllable single-electron tunneling through the junctions gives rise to a direct conversion between the electrostatic energy and that of microwave photons. The measured power spectral density of the microwave radiation emitted by the resonator exceeds at high bias voltages that of an equivalent single-mode radiation source at 2.5 K although the phonon and electron reservoirs are at subkelvin temperatures. Measurements of the generated power quantitatively agree with a theoretical model in a wide range of bias voltages. Thus, we have developed a microwave source which is compatible with low-temperature electronics and offers convenient *in-situ* electrical control of the incoherent photon emission rate with a predetermined frequency, without relying on intrinsic voltage fluctuations of heated normal-metal components or suffering from unwanted losses in room temperature cables. Importantly, our observation of negative generated power at relatively low bias voltages provides a novel type of verification of the working principles of the recently discovered quantum-circuit refrigerator.

Superconducting circuits provide a promising platform for quantum technological applications[1], such as quantum information processing[2–8], sensing[9–11], and refrigeration of electric components[12–15]. In particular, microwave photons constitute a fundamental and controllable medium[16] for energy and information transport between quantum electric components. For example, quantum-limited heat conduction mediated by microwave photons has been measured[13,17], even through coplanar waveguides (CPW) across macroscopic distances[18].

In this framework, both incoherent and coherent microwave sources on the same chip with their target are highly desirable since they minimize unwanted and difficult-to-calibrate losses which typically occur in microwave cables and connectors. Such an incoherent source with high dynamic range can provide reference power with a given frequency for calibration of cryogenic devices[19] such as microwave photon detectors[10] and for experiments on photon statistics[20], thermal transport[15], and quantum-limited amplifiers[21]. A coherent on-chip source[22,23] on the other hand, can potentially be used to drive qubits in the emerging large-scale quantum computers without detrimental heat loads from microwave lines between different temperature stages of the cryostat. Thus, on-chip creation of microwave photons[24–26] and improvement of the dynamic range of the sources are of great interest to electric quantum circuits.

It is well known that tunneling of electrons across a nanoscale barrier can lead to simultaneous energy exchange with the coupled electromagnetic environment such as a resonator[14,15,19,27–39]. Consequently, several schemes for exciting the resonator based on this kind of photon-assisted electron tunneling have been introduced using, for example, Josephson junctions[22,23,40,41] and quantum dots[42–45] (see also[46–49] for schemes utilizing

[1]QCD Labs, QTF Centre of Excellence, Department of Applied Physics, Aalto University, PO Box 13500, AALTO, FI-00076, Finland. [2]Research Unit of Theoretical Physics, University of Oulu, Oulu, FI-90014, Finland. [3]Department of Physics, University of Freiburg, Freiburg im Breisgau, Germany. Correspondence and requests for materials should be addressed to S.M. (email: masulas@tmd.ac.jp) or M.M. (email: mikko.mottonen@aalto.fi)
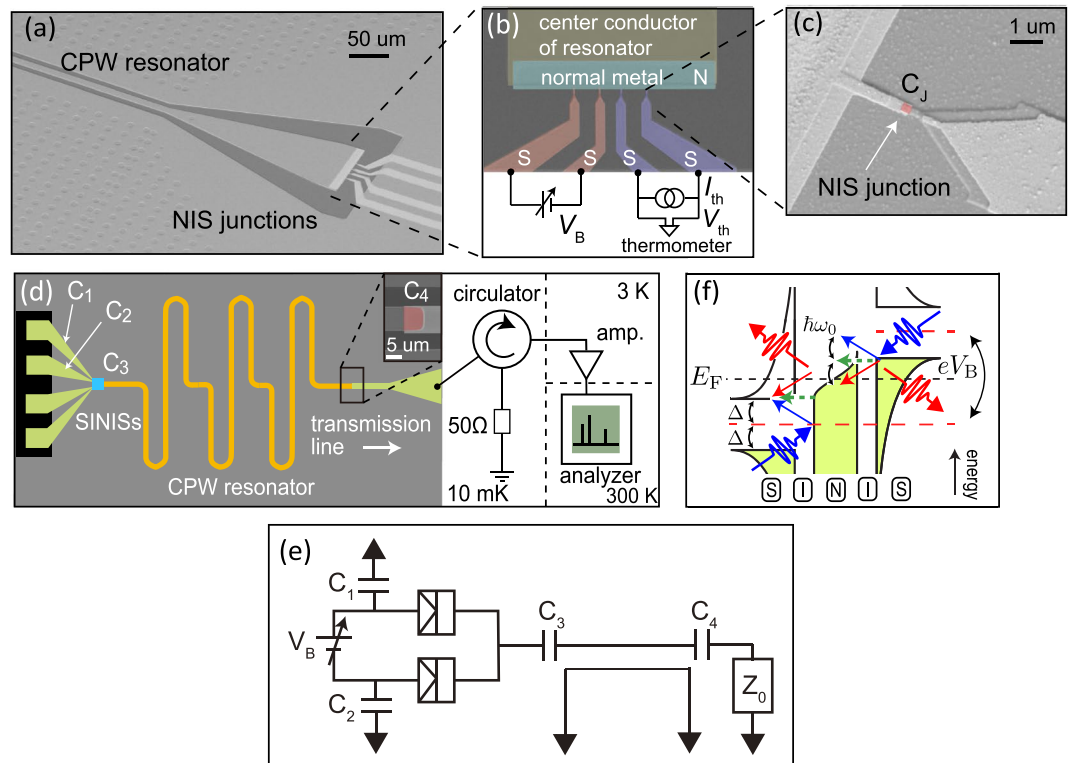
Figure 1. (**a**) Scanning-electron microscope (SEM) image of a fabricated device illustrating the CPW resonator and the NIS junctions operating together as the microwave source. (**b**) Colored SEM image of the NIS junctions. The leads highlighted in red are used to excite the resonator using the bias voltage V_B. The leads highlighted in blue are used as a thermometer to measure the electron temperature of the normal-metal island. (**c**) SEM image of an NIS junction highlighted in red, where C_J denotes the junction capacitance. (**d**) Device design and measurement scheme. Here, C_{1-2}, C_3, and C_4 denote the coupling capacitances between the bonding pads and the ground plane, between the normal-metal island of the NIS junctions and the center conductor of the resonator, and between the resonator and the transmission line (see inset), respectively. The area indicated by the blue square corresponds to panel (a) although the axis of view is different. (**e**) Simplified circuit diagram showing the connections of the labeled components in (d). Here, $Z_0 \simeq 50\,\Omega$ is the characteristic impedance of the transmission line. (**f**) Energy diagram for single-electron tunneling at bias voltage $eV_B/(2\Delta) > 1$, where $\hbar\omega_0$ is the energy of an emitted or absorbed photon. The black solid curves at the normal metal and the superconductors represent the Fermi–Dirac distribution function and the density of states in the superconductors, respectively. The colored areas represent the occupied states. The straight arrow represents the electron tunneling from the initial energy state (beginning of the arrow) to a final energy state (end of the arrow). The wavy arrows denote absorbed or emitted photons in the tunneling process.

superconducting qubits). In contrast, refrigeration of a superconducting microwave resonator mode has been recently demonstrated using voltage-controlled tunneling of single electrons across normal-metal–insulator–superconductor (NIS) tunnel junctions[14]. To the best of our knowledge, however, no microwave source based on metallic NIS tunnel junctions has been demonstrated to date.

In this paper, we report the observation of microwave absorption and emission arising from photon-assisted single-electron tunneling through NIS junctions. The experimental setup is extended from that of the first quantum-circuit refrigerator[14], such that we can measure the power spectral density of the microwave radiation generated in a CPW resonator. The device is compatible with low-temperature electronics and offers orders of magnitude electrical tunability of the generated power with the frequency corresponding to the lowest mode of the CPW resonator. Importantly, we observe that the resonator mode is cooled by the quantum-circuit refrigerator by measuring for the first time the effect of the refrigerator on the emitted radiation. Furthermore, our results demonstrate that the mode temperature of the resonator can be driven beyond 2.5 K, far above the temperatures of the phonon and electron reservoirs of the system. Thus when operated as an incoherent microwave source, our device has potential in delivering relatively high powers without the excess heating of other nearby components or sensitivity to modest external magnetic fields.

Results and Discussion

The experimental sample shown in Fig. 1(a)–(c) consists of NIS tunnel junctions capacitively coupled to a half-wave-length superconducting CPW resonator fabricated on a high-purity 500-μm-thick silicon wafer. The silicon substrate is passivated with a 300-nm-thick thermally grown silicon dioxide. The resonator is defined with

2

photolithography and reactive ion etching of a 200-nm-thick sputtered Nb layer. Subsequently, a 50-nm-thick layer of Al_2O_3 is introduced on the whole wafer using atomic layer deposition (ALD) process at 200 °C. This ALD oxide serves as the dielectric material of the parallel plate capacitors C_{1-4} shown in Fig. 1(d). The NIS junctions and a transmission line connected to the resonator are subsequently defined using electron beam lithography, followed by a standard two-angle evaporation with *in-situ* oxidation to form the tunnel barriers. The final NIS nano-structure consists of a 20-nm-thick normal metal (Cu) on top of a 20-nm-thick superconductor (Al), separated by a thin aluminum-oxide tunnel barrier. The tunnel junction area is approximately $200 \times 200 \, nm^2$ inferred from the SEM image of the sample.

Figure 1(d) depicts the layout of the sample and the measurement setup with a simplified circuit diagram given in Fig. 1(e) (see Sec. III of Supplementary information for more details). Microwave photons generated in the resonator at 10-mK cryostat temperature decay into the transmission line, and are characterized using a spectrum analyzer. As depicted in Fig. 1(b), a pair of voltage-biased NIS junctions is used to create the photons, while a current-biased pair is used as a thermometer to measure the electron temperature of the normal-metal island[50] (see Sec. V of Supplementary information). To estimate the power generated by controlled electron tunneling without offsets, we subtract the measured power corresponding to the off-state of the source, namely, zero bias voltage, from the power measured at finite bias voltages. We refer to this quantity as the generated power.

To enhance the interaction between the tunneling electrons and the resonator, we use a large coupling capacitance between the normal-metal island and the resonator, C_3, in comparison to the tunnel junction capacitance, C_J. For the sake of convenient experimental detection, the coupling capacitance between the resonator and the transmission line is chosen to maintain a well-defined resonance although with a relatively low loaded resonator quality factor $Q \approx 60$. Note that the source may also be conveniently designed for narrow-bandwidth operation. The resonator length is chosen to obtain the desired frequency of the generated radiation. In this work, we examine two samples with resonator lengths of $L_{res} = 13.14$ mm (Sample A) and 6.89 mm (Sample B) which correspond to the fundamental resonance frequencies of 4.55 GHz and 8.32 GHz, respectively.

Although elastic tunneling, where the electron does not exchange energy with the resonator, is typically frequent in our experiments, photon-assisted electron tunneling is the key phenomenon leading to the photon creation we observe below. When an electron tunnels across an NIS junction, it can absorb energy from or emit energy to the resonator, that is, annihilate or create photons in the resonator[30]. Figure 1(f) illustrates elastic and photon-assisted single-electron tunneling events across the junctions and the associated photon creation and annihilation. If the energy provided by the bias voltage to the electron tunneling across the junction, $eV_B/2$, is greater than the superconductor gap parameter, Δ, the photon creation rate increases faster with the bias voltage than the annihilation rate. Thus, the effective temperature related to the creation and annihilation of photons increases. The elastic tunneling does not directly affect the resonator modes but typically dominates the electric current across the junctions for $eV_B/2 \gtrsim \Delta$.

Figure 2(a) and (b) show the spectral density of the generated power as a function of the bias voltage for Sample A. We observe increased generated power around 4.55 GHz matching the frequency of the fundamental resonator mode estimated using the experimental parameters given in Table 1. The spectral brightening can be mostly described by a characteristic Lorenzian peak. We attribute the additional structure to microwave reflections from the circuitry following the resonator.

The power spectral density increases with the bias voltage for $|eV_B/(2\Delta)| > 1$ whereas it is almost vanishing for $|eV_B/(2\Delta)| < 1$. This onset of generated radiation matching the energy gap in the superconductor density of states provides clear evidence that single-electron tunneling is responsible for the observed photon emission. In the units of the photon emission rate per hertz, the observed maximum power spectral density of roughly $80 \, Hz^{-1}s^{-1}$ at $eV_B/(2\Delta) \simeq 14$ is orders of magnitude higher than those reported in refs[41,43] for incoherent sources. Some coherent sources[22,23] provide yet orders of magnitude higher power spectral density. However, our incoherent source is based on a different physical phenomenon. Thus, its output power has a simple bias-voltage dependence, offering robust *in-situ* electrical control. The bias-voltage dependence of the frequency-integrated spectral density, i.e., the generated power is shown in Fig. 2(c). The onset of positive generated power is clearly visible at $eV_B/(2\Delta) \gtrsim 1$.

Owing to energy conservation, the net power flowing from the resonator to the transmission line is given by $P_{RT} = P_{out} - P_{in}$, where P_{out} and P_{in} are the powers carried by photons moving in the transmission line away from and towards the microwave source, respectively. The net power is related to the average photon number of the resonator, $\bar{n}_{res}$, and of the radiation incident on the resonator from the transmission line, $\bar{n}_{TL}$, at the fundamental angular frequency, ω_0, by (see Sec. IV of Supplementary information)

$$P_{RT} = \frac{2C_4^2 \hbar \omega_0^3 Z_0}{L_{res} c_{res}} (\bar{n}_{res} - \bar{n}_{TL}),$$

(1)

where Z_0 is the characteristic impedance of the transmission line and c_{res} is the capacitance per unit length of the resonator. The circulator shown in Fig. 1(d) renders P_{in} and $\bar{n}_{TL}$ independent of the bias voltage, and hence the generated power assumes the form

$$\Delta P_{out} := P_{out}(V_B) - P_{out}(0) = \frac{2C_4^2 \hbar \omega_0^3 Z_0}{L_{res} c_{res}} [\bar{n}_{res}(V_B) - \bar{n}_{res}(0)].$$

(2)

Although the above equation only provides a direct conversion from the measured generated power to the change of the average resonator photon number, we describe in Sec. IV of Supplementary information how we extract the photon number at zero bias with the help of our theoretical model. In the model, we assume for
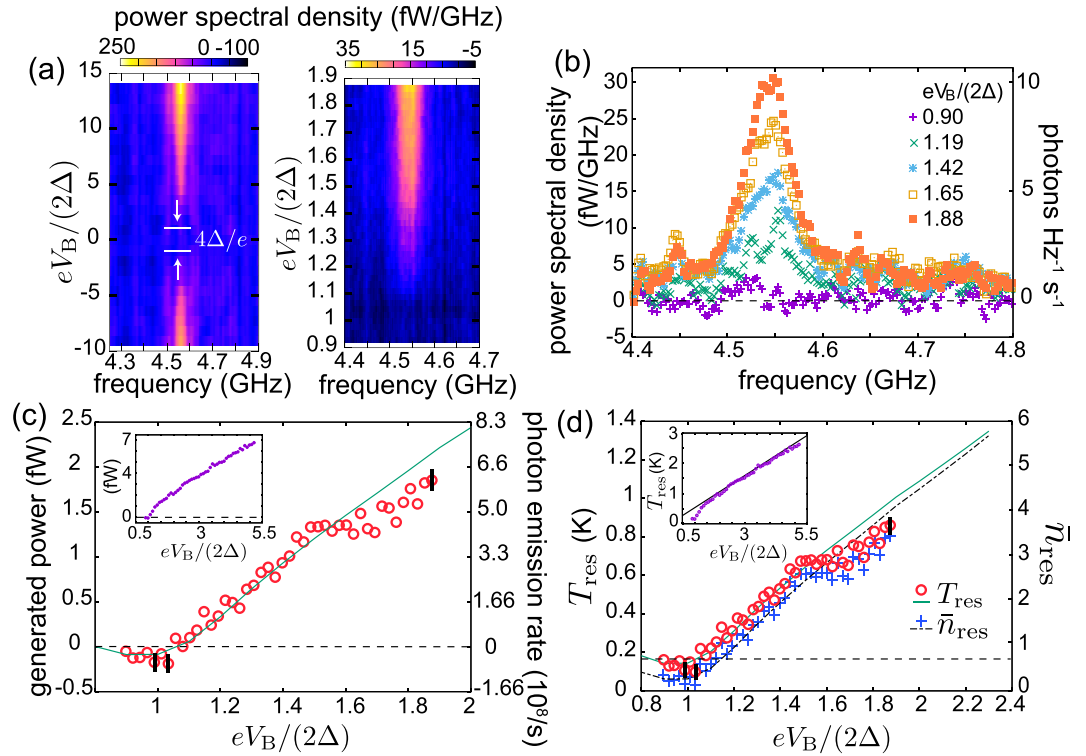
Figure 2. Experimental and numerical results for Sample A with the fundamental resonance frequency $f_0 =$ 4.55 GHz. (**a**) Spectral densities of the generated power measured as functions of frequency and bias voltage. Each frequency trace is measured by a spectrum analyzer as shown schematically in Fig. 1(d) and averaged over 21000 repetitions. In addition, we employ a three-point moving average in frequency. The left panel shows the generated power spectral density in a wider voltage range compared with the right panel. In contrast to Fig. 1(d), no circulator was used for the data in the left panel. (**b**) Power spectral density and the corresponding density of photon emission rate (photons Hz^{-1} s^{-1}) of (a) as functions of frequency for the indicated bias voltages. The horizontal dashed line indicates the zero level corresponding to zero bias voltage. (**c**) Generated power, obtained by integrating data as in (b) from 4.4 GHz to 4.8 GHz. The green curve indicates the theoretical prediction of the thermal model illustrated in Fig. 3. The inset shows the generated power for an extended bias voltage range. The dashed lines indicate the zero level. (**d**) Average photon number and temperature of the fundamental mode as functions of the bias voltage obtained using the experimental results in (c) and Eqs (2) and (3). The parameters are given in Table 1. Here, the dashed and solid curves represent $\bar{n}_{res}$ and T_{res} obtained from the thermal model, respectively. Representative 1σ uncertainties of the measured data points are shown by black vertical lines in (c) and (d). The solid line in the inset of (d) represents $T_{res} = eV_B/(4k_B + 2k_B R_T Z_0 C_4^2 \omega_0^2)$, which is obtained in the high voltage regime where $\bar{n}_{res} \approx k_B T_{res}/(\hbar\omega_0)$[51]. We used a 38.5-dB cryogenic amplifier, 20-dB room temperature amplifier, and 6-dB room temperature attenuator. We assumed 11.9 dB of loss from the PCB and rf cables as opposed to 7.5 dB calibrated with a transmission measurement of a control sample. We attribute the discrepancy in the loss mainly to the fact that the microwaves propagate through additional cables in the calibration measurement, which leads to excess uncertainties. The horizontal dashed line indicates the apparent temperature of the transmission line as given in Table 1.

simplicity that the exchanged power P_{RT} vanishes at zero bias voltage, i.e., here the resonator is thermalized with the transmission line. This assumption does not lead to artificial changes in the estimated $\bar{n}_{res}$, but renders $\bar{n}_{TL}$ to describe the joint voltage-bias-independent heating effect of the resonator owing to the transmission line and any additional environments. Consequently, we refer below to T_{TL} as the apparent transmission line temperature. Note that the estimated resonator temperature becomes insensitive to changes in T_{TL} at high bias voltages where $\bar{n}_{res} \gg \bar{n}_{TL}$. In our experiments, the resonator mode is in a thermal state described by temperature T_{res}, and hence we may describe its average photon numbers using the Bose distribution function as

$$\bar{n}_{res} = \frac{1}{\exp[\hbar\omega_0/(k_B T_{res})] - 1}.$$ (3)

Figure 2(d) shows the resonator temperature and average photon number corresponding to the measured generated power in Fig. 2(c) as functions of the bias voltage. These results indicate that the mode temperature and the average photon number can be efficiently controlled using the bias voltage. For $eV_B > 10\Delta$, we have $T_{res} > 2.5$ K. Such a high mode temperature is not conveniently achieved by coupling the resonator to a hot resistor due to the transition of the superconducting aluminum, employed as the lead material, to the normal state.

	SAMPLE A	SAMPLE B		SAMPLE A	SAMPLE B
L_{res}	13.14 mm	6.89 mm	C_3	0.84 pF	0.78 pF
Δ	220 μeV	191 μeV	C_4	0.072 pF	0.079 pF
γ_{D}	4×10^{-4}	4×10^{-4}	Z_0	53 Ω	52 Ω
c_{res}	159 pF/m	169 pF/m	T_{TL}	180 mK	150 mK
l_{res}	0.45 μH/m	0.45 μH/m	α	11.9 dB[a]	17 dB[b]
f_0	4.55 GHz	8.32 GHz	w	7.8 μm	8.0 μm
R_{T}	12.5 kΩ	10.0 kΩ	s	5.7 μm	6.1 μm
C_{J}	2 fF	2 fF			

Table 1. Parameters of the experimental samples (see Sec. II of Supplementary information for details): the length of the resonator L_{res}, superconductor gap parameter Δ, Dynes parameter γ_{D}, capacitance per unit length c_{res}, inductance per unit length l_{res}, fundamental resonance frequency f_0, tunnel resistance R_{T}, junction capacitance C_{J}, capacitance $C_{3/4}$, characteristic impedance of the transmission line Z_0, apparent temperature of transmission line T_{TL}, the employed attenuation of the PCB and rf cables α, the width of the center conductor w, and the separation between the center conductor and the ground plane of the CPW resonator s. Capacitance $C_{1/2}$ is more than 50 times larger than C_3. [a,b]The values experimentally measured with a control sample are 7.5 dB[a] and 13 dB[b].
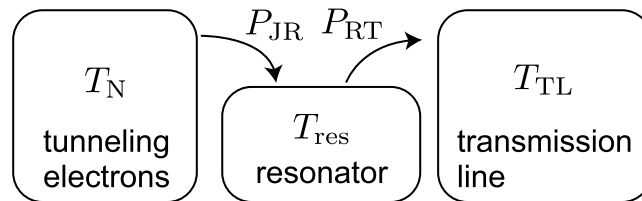

Figure 3. Thermal model of the device indicating the relevant temperatures and energy flows. The temperature of the fundamental resonator mode, T_{res}, becomes higher than the apparent temperature of the transmission line, T_{TL}, when the applied bias voltage strongly drives photon creation. Here, T_{N} is the electron temperature at the normal-metal island of the NIS junctions. At steady state, the power P_{JR} from the tunneling electrons to the resonator and the power P_{RT} from the resonator to the transmission line balance, $P_{\text{JR}} = P_{\text{RT}}$. See Sec. III and IV of Supplementary information for details on modeling the power flows.

Importantly, the measured electron temperature shown in Sec. V of Supplementary information is much lower than that of the resonator mode for almost any bias voltage in Fig. 2(d). This observation verifies that the observed microwave radiation directly arises from photon-assisted electron tunneling rather than from heating of the normal-metal island.

Although negative generated power is challenging to differentiate in the measured power spectra, we observe in Fig. 2(c) a shallow but statistically significant dip in the experimental generated power around $eV_{\text{B}}/(2\Delta) = 1$. The dip corresponds to the refrigeration of the fundamental mode owing to photon-assisted tunneling, and hence provides complementary evidence of this phenomenon first observed in ref.[14]. As theoretically shown in refs[14,51], the photon-assisted tunneling acts on the resonator as an environment, the effective temperature of which achieves a minimum of half the electron temperature somewhat below the gap voltage. This qualitatively explains the observed refrigeration. At high bias voltages, the effective temperature approaches $eV_{\text{B}}/(2k_{\text{B}})$[51], and hence a local minimum in the generated power appears.

To describe the energy transfer from the tunneling electrons to the transmission line, mediated by microwave photons in the fundamental mode of the resonator, we develop a thermal model shown in Fig. 3. Here, we consider thermal states for the electric components assuming that the temperatures of the resonator mode, T_{res}, and of the electrons in the normal-metal island, T_{N}, are well defined in the parameter range studied. We have verified the validity of this assumption with a model that accounts for transitions between individual resonator states[51] but do not present the model here since its predictions are essentially identical to those provided by our simpler model. Because of the relatively weak coupling between the resonator and the transmission line, we assume that a tunneling electron does not induce photon-assisted transitions in the transmission line. Instead, the influence of the tunneling events is indirectly taken into account through the change in the temperature of the resonator mode.

In the thermal model, the power from the tunneling electrons to the resonator, P_{JR}, is calculated using the $P(E)$ theory[30], as detailed in Sec. III of Supplementary information. Both powers, P_{JR} and P_{RT}, are functions of the temperature of the resonator mode. We solve P_{RT} for each V_{B} by finding the mode temperature, at which these powers balance, $P_{\text{JR}} = P_{\text{RT}}$. Subsequently, the average photon number $\bar{n}_{\text{res}}$ is calculated using the obtained mode temperature and Eq. (3). We have measured the bare internal quality factor of samples with the same design to be orders of magnitude higher than the realized external quality factor and hence we neglect the effect of any additional internal losses to the power balance. The apparent temperature of the transmission line, corresponding to the photons
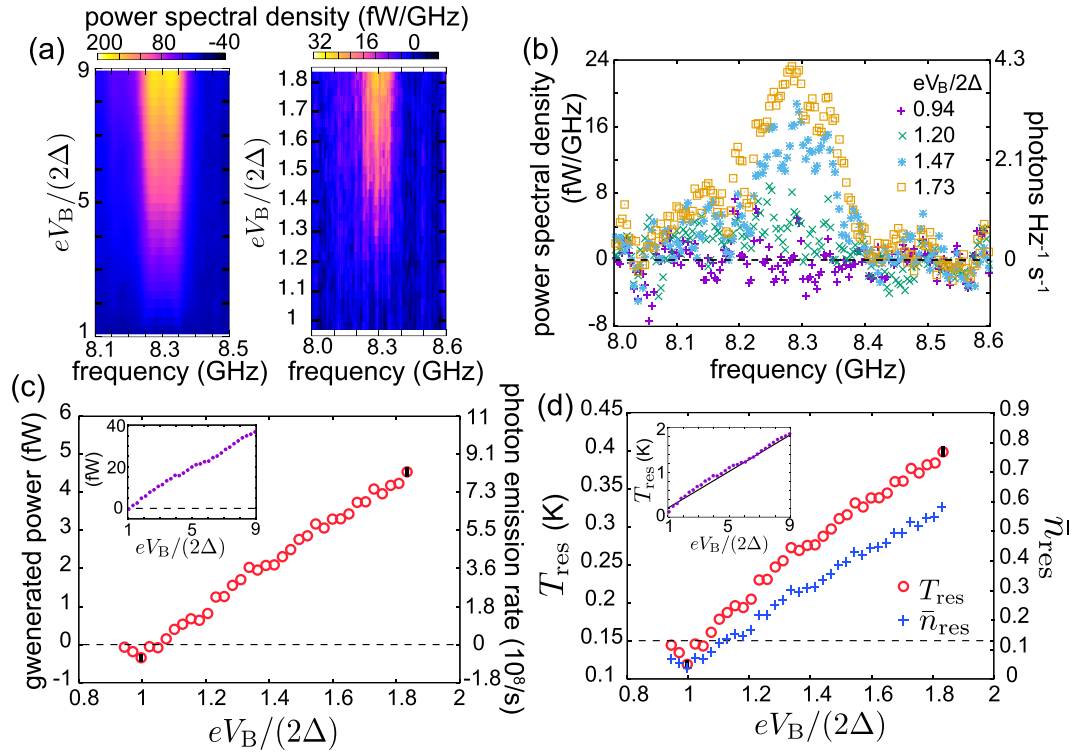
Figure 4. Experimental results for Sample B with the fundamental resonance frequency $f_0 = 8.3$ GHz. (**a**) Spectral densities of the generated power measured as functions of frequency and bias voltage. The left panel shows the generated power spectral density in a wider voltage range compared with the right panel. (b) Power spectral density and the corresponding density of photon emission rate (photons $Hz^{-1} s^{-1}$) of (a) as functions of frequency for the indicated bias voltages. The horizontal dashed line indicates the zero level. (**c**) Generated power, obtained by integrating data as in (b) from 8.0 GHz to 8.6 GHz. The inset shows the generated power for an extended bias voltage range. The dashed lines indicate the zero levels. (**d**) Average photon number and temperature of the fundamental mode as functions of the bias voltage obtained using the data in (c) and Eqs (2) and (3). The parameters are given in Table 1. Representative 1σ uncertainties of the measured data points are shown by black vertical lines in (c) and (d). The solid line in the inset of (d) represents $T_{res} = eV_B/(4k_B + 2k_B R_T Z_0 C_4^2 \omega_0^2)$, which is obtained in the high voltage regime where $\bar{n}_{res} \approx k_B T_{res}/(\hbar\omega_0)$[51]. We used a 40-dB cryogenic amplifier, 20-dB room temperature amplifier, and 6-dB room temperature attenuator. We assumed 17 dB of loss from the PCB and rf cables as opposed to 13 dB measured using a control sample. The horizontal dashed line indicates the apparent temperature of the transmission line as given in Table 1. In contrast to Fig. 2(c) and (d), we do not show theoretical results here due to the lack of reliable temperature data for the normal-metal electrons.

moving towards the resonator and possible additional heating channels, is assumed to be independent of the applied bias voltage. The experimentally measured electron temperature of the normal-metal island is used in the simulation.

The theoretical results, employing the parameters given in Table 1, show in Fig. 2(c) good agreement with the experiments in a wide range of generated powers. In the model, the dip in the generated power around $eV_B/(2\Delta) = 1$ is arising from photon absorption induced by electron tunneling. Furthermore, the modelled average number of photons, $\bar{n}_{res}$, and the temperature of the fundamental mode, T_{res}, are shown in Fig. 2(d) as functions of the bias voltage.

Experimental results similar to those discussed above are shown in Fig. 4 for Sample B. Figure 4(a) shows the spectral density of the generated power as a function of the frequency and the bias voltage. A peak appears around 8.3 GHz for $eV_B/(2\Delta) > 1$ and becomes taller with increasing bias voltage. Figure 4(b) exhibits the traces of the spectral density, which are integrated for Fig. 4(c) to obtain the generated power as a function of the bias voltage. The qualitative behavior of the generated power matches that of Sample A: the power begins to increase with bias voltage around $eV_B/(2\Delta) = 1$, where we observe a shallow dip corresponding to cooling of the resonator. However, the magnitude of the generated power is greater and the mode temperature shown in Fig. 4(d) is lower compared with Fig. 2. This is because the coupling of the resonator to the transmission line is proportional to the third power of the resonance frequency [see Eq. (1)] which is almost twice as large here in comparison to Sample A.

Conclusions

We observed microwave absorption and emission arising from photon-assisted single-electron tunneling through NIS junctions. We experimentally verified cooling by the quantum-circuit refrigerator[14] by measuring for the first time the power spectral density of microwaves emitted from the resonator. Furthermore, we have implemented

6

an incoherent microwave source which realizes direct conversion of the electrostatic energy provided by the dc voltage source to microwave photons. Importantly, it does not rely on the thermal voltage fluctuation spectrum of a resistor, and much like shot-noise sources[19,39], it may provide higher effective temperatures, faster tunability, and less excess heating than usual thermal methods. Our measurements of the generated power are in good agreement with the corresponding theoretical model, heavily suggesting that our interpretation that photon-assisted tunneling is mainly responsible for the generated power is correct. This interpretation is verified by the observation of much higher generated powers than what is expected for resonator temperatures matching the normal-metal electron temperature. In the future, we aim to extend this photon source to narrow bandwidths and pulsed operation. In an effort to obtain a stringent quantitative verification of the validity of the used theoretical model, we aim to measure the characteristics of the source using a cryogenic microwave bolometer[10] or a qubit coupled to the resonator[52].

References

1. Wolf, E. L. *Quantum Nanoelectronics: An Introduction to Electronic Nanotechnology and Quantum Computing* (Wiley-VCH, Weinheim, 2009).
2. Blais, A., Huang, R.-S., Wallraff, A., Girvin, S. M. & Schoelkopf, R. J. Cavity Quantum Electrodynamics for Superconducting Electrical Circuits: an Architecture for Quantum Computation. *Phys. Rev. A* **69**, 062320 (2004).
3. Wallraff, A. *et al.* Strong Coupling of a Single Photon to a Superconducting Qubit using Circuit Quantum Electrodynamics. *Nature* **431**, 162–167 (2004).
4. Majer, J. *et al.* Coupling Superconducting Qubits via a Cavity Bus. *Nature* **449**, 443–447 (2007).
5. Sillanpää, M. A., Park, J. I. & Simmonds, R. W. Coherent Quantum State Storage and Transfer between Two Phase Qubits via a Resonant Cavity. *Nature* **449**, 438–442 (2007).
6. Devoret, M. H. & Schoelkopf, R. J. Superconducting Circuits for Quantum Information: an Outlook. *Science* **339**, 1169–1174 (2013).
7. Kelly, J. *et al.* State Preservation by Repetitive Error Detection in a Superconducting Quantum Circuit. *Nature* **519**, 66–69 (2015).
8. Ofek, N. *et al.* Extending the Lifetime of a Quantum Bit with Error Correction in Superconducting Circuits. *Nature* **536**, 441–445 (2016).
9. Inomata, K. *et al.* Single Microwave-Photon Detector using an Artificial Λ-Type Three-Level System. *Nat. Commun.* **7**, 12303 (2016).
10. Govenius, J., Lake, R. E., Tan, K. Y. & Möttönen, M. Detection of Zeptojoule Microwave Pulses using Electrothermal Feedback in Proximity-Induced Josephson Junctions. *Phys. Rev. Lett.* **117**, 030802 (2016).
11. Saira, O.-P., Zgirski, M., Viisanen, K. L., Golubev, D. S. & Pekola, J. P. Dispersive Thermometry with a Josephson Junction Coupled to a Resonator. *Phys. Rev. Applied* **6**, 024005 (2016).
12. Clark, A. M. *et al.* Cooling of Bulk Material by Electron-Tunneling Refrigerators. *Appl. Phys. Lett.* **86**, 173508–173510 (2005).
13. Timofeev, A. V., Helle, M., Meschke, M., Möttönen, M. & Pekola, J. P. Electronic Refrigeration at the Quantum Limit. *Phys. Rev. Lett.* **102**, 200801 (2009).
14. Tan, K. Y. *et al.* Quantum-circuit Refrigerator. *Nat. Commun.* **8**, 15189 (2017).
15. Giazotto, F., Heikkilä, T. T., Luukanen, A., Savin, A. M. & Pekola, J. P. Opportunities for Mesoscopics in Thermometry and Refrigeration: Physics and Applications. *Rev. Mod. Phys.* **78**, 217–274 (2006).
16. Hofheinz, M. *et al.* Synthesizing Arbitrary Quantum States in a Superconducting Resonator. *Nature* **459**, 546–549 (2009).
17. Meschke, M., Guichard, W. & Pekola, J. P. Single-mode Heat Conduction by Photons. *Nature* **444**, 187–190 (2006).
18. Partanen, M. *et al.* Quantum-Limited Heat Conduction over Macroscopic Distances. *Nat. Phys.* **12**, 460–464 (2016).
19. Spietz, L. *et al.* Primary Electronic Thermometry Using the Shot Noise of a Tunnel Junction. *Science* **300**, 1929–1932 (2003).
20. Goetz, J. *et al.* Photon Statistics of Propagating Thermal Microwaves. *Phys. Rev. Lett.* **118**, 103602 (2016).
21. Spietz, L. *et al.* Noise performance of lumped element direct current superconducting quantum interference device amplifiers in the 4–8 GHz range. *Applied Phys. Lett.* **97**, 142502 (2010).
22. Chen, F. *et al.* Realization of a single-Cooper-pair Josephson laser. *Phys. Rev. B* **90**, 020506 (2014).
23. Cassidy, M. C. *et al.* Demonstration of an ac Josephson junction laser. *Science* **355**, 939–942 (2017).
24. Houck, A. A. *et al.* Generating Single Microwave Photons in a Circuit. *Nature* **449**, 328–331 (2007).
25. Bozyigit, D. *et al.* Antibunching of microwave-frequency photons observed in correlation measurements using linear detectors. *Nat. Phys.* **7**, 154–158 (2011).
26. Peng, Z. H., de Graaf, S. E., Tsai, J. S. & Astafiev, O. V. Tuneable on-demand single-photon source in the microwave range. *Nat. Commun.* **449**, 12588 (2016).
27. Devoret, M. H. *et al.* Effect of the Electromagnetic Environment on the Coulomb Blockade in Ultrasmall Tunnel Junctions. *Phys. Rev. Lett.* **64**, 1824 (1990).
28. Girvin, S. M., Glazman, L. I., Jonson, M., Penn, D. R. & Stiles, M. D. Quantum Fluctuations and the Single-Junction Coulomb Blockade. *Phys. Rev. Lett.* **64**, 3183 (1990).
29. Averin, B., Nazarov, Y. & Odintsov, A. Incoherent Tunneling of the Cooper Pairs and Magnetic Flux Quanta in Ultrasmall Josephson Junctions. *Physica B* **165/166**, 945–946 (1990).
30. Ingold, G.-L. & Nazarov, Y. V. Charge Tunneling Rates in Ultrasmall Junctions. *NATO ASI Series B* **294**, 21–107 (1992).
31. Holst, T., Esteve, D., Urbina, C. & Devoret, M. H. Effect of a Transmission Line Resonator on a Small Capacitance Tunnel Junction. *Phys. Rev. Lett.* **73**, 3455 (1994).
32. Ingold, G.-L., Grabert, H. & Eberhardt, U. Cooper-pair current through ultrasmall Josephson junctions. *Phys. Rev. B* **50**, 395 (1994).
33. Lu, W., Maranowski, K. D. & Rimberg, A. J. Charge transport processes in a superconducting single-electron transistor coupled to a microstrip transmission line. *Phys. Rev. B* **65**(R), 060501 (2002).
34. Billangeon, P.-M. *et al.* Emission and Absorption Asymmetry in the Quantum Noise of a Josephson Junction. *Phys. Rev. Lett.* **96**, 136804 (2006).
35. Toppari, J. J. *et al.* Cooper-pair resonances and subgap Coulomb blockade in a superconducting single-electron transistor. *Phys. Rev. B* **76**, 172505 (2007).
36. Billangeon, P.-M., Pierre, F., Bouchiat, H. & Deblock, R. ac Josephson Effect and Resonant Cooper Pair Tunneling Emission of a Single Cooper Pair Transistor. *Phys. Rev. Lett.* **98**, 216802 (2007).
37. Pekola, J. P. *et al.* Environment-Assisted Tunneling as an Origin of the Dynes Density of States. *Phys. Rev. Lett.* **105**, 026803 (2010).
38. Pashkin, Yu. A. *et al.* Charge transport through ultrasmall single and double Josephson junctions coupled to resonant modes of the electromagnetic environment. *Phys. Rev. B* **83**(R), 020502 (2011).
39. Gabelli, J. *et al.* Electron-photon correlations and the third moment of quantum noise. *New J. Phys.* **15**, 113045 (2013).
40. Zakka-Bajjani, E. *et al.* Experimental Determination of the Statistics of Photons Emitted by a Tunnel Junction. *Phys. Rev. Lett.* **104**, 206802 (2010).
41. Hofheinz, M. *et al.* Bright Side of the Coulomb Blockade. *Phys. Rev. Lett.* **106**, 217005 (2011).
42. Bruhat, L. E. *et al.* Cavity Photons as a Probe for Charge Relaxation Resistance and Photon Emission in a Quantum Dot Coupled to Normal and Superconducting Continua. *Phys. Rev. X* **6**, 021014 (2016).

43. Stockklauser, A. *et al.* Microwave Emission from Hybridized States in a Semiconductor Charge Qubit. *Phys. Rev. Lett.* **115**, 046802 (2015).
44. Childress, L., Sørensen, A. S. & Lukin, M. D. Mesoscopic Cavity Quantum Electrodynamics with Quantum Dots. *Phys. Rev. A* **69**, 042302 (2004).
45. Liu, Y.-Y., Petersson, K. D., Stehlik, J., Taylor, J. M. & Petta, J. R. Photon Emission from a Cavity-Coupled Double Quantum Dot. *Phys. Rev. Lett.* **113**, 036801 (2014).
46. You, J. Q., Liu, Y. X., Sun, C. P. & Nori, F. Persistent Single-Photon production by Tunable On-chip Micromaser with a Superconducting Quantum Circuit. *Phys. Rev. B* **75**, 104516 (2007).
47. Astafiev, O. *et al.* Single Artificial-Atom Lasing. *Nature* **449**, 588–590 (2007).
48. Hauss, J., Fedorov, A., Hutter, C., Shnirman, A. & Schön, G. Single-Qubit Lasing and Cooling at the Rabi Frequency. *Phys. Rev. Lett.* **100**, 037003 (2008).
49. Grajcar, M. *et al.* Sisyphus Cooling and Amplification by a Superconducting Qubit. *Nat. Phys.* **4**, 612–616 (2008).
50. Leivo, M. M., Pekola, J. P. & Averin, D. V. Efficient Peltier Refrigeration by a Pair of Normal Metal/Insulator/Superconductor Junctions. *Appl. Phys. Lett.* **68**, 1996–1998 (1996).
51. Silveri, M., Grabert, H., Masuda, S., Tan, K. Y. & Möttönen, M. *Phys. Rev. B* **96**, 094524 (2017).
52. Suri, B. *et al.* Nonlinear microwave photon occupancy of a driven resonator strongly coupled to a transmon qubit. *Phys. Rev. A* **92**, 063801 (2015).

Acknowledgements

Author Contributions

S.M. and K.Y.T. fabricated the samples and conducted the experiments. S.M. also developed the model and analysed the data. M.P. contributed to the sample fabrication, measurements, and data analysis. R.L. and J.G. contributed to the measurements. M.S. and H.G. contributed to the theoretical analysis. M.M. provided the initial ideas and suggestions for the experiment, and supervised the work in all respects. All authors commented on the manuscript written by S.M. and M.M.

Additional Information

Supplementary information accompanies this paper at https://doi.org/10.1038/s41598-018-21772-5.

Competing Interests: The authors declare no competing interests.

Publisher's note: Springer Nature remains neutral with regard to jurisdictional claims in published maps and institutional affiliations.